Journal of Materials Chemistry A

ROYAL SOCIETY OF CHEMISTRY

PAPER

View Article Online
View Journal | View Issue

Cite this: J. Mater. Chem. A, 2022, 10, 12473

Hierarchical pipe cactus-like Ni/NiCo-LDH core–shell nanotube networks as a self-supported battery-type electrode for supercapacitors with high volumetric energy density†

Khaled M. Amin, *[ab] Konrad Krois,[c] Falk Muench,[d] Bastian J. M. Etzold [c] and Wolfgang Ensinger[a]

High-performance yet thin hybrid supercapacitors (HSC) are urgently needed to meet the increasing demands of wearable and portable electronic devices. Nevertheless, most of the current electrode designs employed to enhance the electrode capacity and conductivity provide limited volumetric capacity because they commonly rely on macroscopic, heavy support materials such as nickel foam or carbon cloth. Hence, micro- and nanostructuring strategies towards tailored electrode architectures will be vital for their utilization in practical applications. Herein, a three-dimensional (3D) self-supported hierarchical electrode was obtained by directly growing NiCo layered double hydroxide (NiCo-LDH) nanosheets on a Ni nanotube network (Ni-NTNW) *via* electrodeposition. The resulting electrode takes advantage of the large interface and the high redox activity of the two-dimensional (2D) coating nanosheets, whose properties are augmented by the highly porous network architecture of the one-dimensional (1D) Ni-NTNW support, which enables fast mass transfer and acts as a "highway" for fast electron transfer. The fabricated NiCo-LDH@Ni-NTNW architecture replicates the thickness of the parent template (20 μm) employed for the electroless plating of the Ni-NTNW, resulting in an ultrathin battery-type electrode with a superb volumetric capacity of 126.4 C cm^{-3}, remarkable rate capability, and outstanding cycling stability. Additionally, the assembled NiCo-LDH@Ni-NTNW//activated carbon (AC) HSC can deliver a high volumetric capacitance of 76.7 F cm^{-3} at a current density of 1 mA cm^{-2}. Meanwhile, it exhibits a high energy density of 14.7 mWh cm^{-3} with a maximum power density of 4769 mW cm^{-3}, surpassing most state-of-the-art supercapacitors that deliver high volumetric energy density. As such, hybrid core–shell nanotube networks represent an up-and-coming design paradigm for high-performance supercapacitor devices in portable devices.

Received 10th January 2022
Accepted 7th April 2022

DOI: 10.1039/d2ta00235c

rsc.li/materials-a

1 Introduction

The increasing growth in energy consumption during the last few decades raised the demand for clean and renewable energy sources which in turn has stimulated more efforts in developing high-performance energy storage devices, particularly supercapacitors.[1–3] Supercapacitors represent one of the most promising candidates for power devices due to their outstanding power density, superior cycling stability, and fast charge–discharge rates.[4,5] However, the use of supercapacitors in practical applications is still hindered compared to that of lithium-ion batteries due to their low energy density.[6–9] The overall performance of a supercapacitor mainly stems from the electrode architecture and composition. Hence, ongoing efforts are focused on realizing efficient electrode materials and designs that combine outstanding power density and a long lifetime with high energy density within a controlled small size.[10–15] Recent research has reported devices with high specific capacitances, but still, the challenge is to achieve high volumetric capacitance which is a pivotal parameter, especially for the application in wearable devices and smart electronics with a limited space allocated for the energy source.[16–19] The traditional way to enhance the volumetric capacitance is to increase the mass loading of active material per cubic centimeter, which however comes at the cost of an increased dead mass of the electrode, because of missing electrical contact or deterioration of contact during operation due to morphological changes or

[a]Department of Materials Science, Technical University of Darmstadt, Darmstadt 64287, Germany. E-mail: amin@ma.tu-darmstadt.de
[b]Department of Polymer Chemistry, Atomic Energy Authority, Cairo 11787, Egypt
[c]Ernst-Berl-Institut für Technische und Makromolekulare Chemie, Department of Chemistry, Technical University of Darmstadt, Darmstadt 64287, Germany
[d]MagnoTherm Solutions GmbH, Pfungstädter Straße 102, Eberstadt, Darmstadt 64297, Germany

† Electronic supplementary information (ESI) available. See https://doi.org.10.1039/d2ta00235c

stresses breaking off parts of the material and collapse of the three-dimensional (3D) architecture or a less porous electrode layer due to more filling.[16,20] Hence, optimization of the electrode architecture is very important to maximize the performance in terms of volumetric capacitance and energy density within the same electrode geometry and without increasing the mass loading.

Supercapacitors are classified based on the energy storage mechanism of the electrode material into three classes: double-layer capacitors, pseudocapacitors, and battery-type capacitors. Among them, the battery-type capacitors have recently attracted considerable attention because of their high capacities and short ion-diffusion paths.[21] Battery-type electrode materials include transition metal hydroxides, sulfides, phosphides, selenides, and oxides which have been extensively investigated as electrode materials for hybrid supercapacitors (HSC), delivering higher energy density than double-layer capacitors.[22–30] The last few years witnessed a surge in employing metal layered double hydroxides (LDH), particularly NiCo-LDH as a battery-type electrode material with its layered structure, high redox activity, and outstanding anion exchange, which enhance the charge storage.[31–33] Moreover, the synergy between $Ni(OH)_2$ with its high theoretical specific capacity and $Co(OH)_2$ with its good electrical conductivity plays an important role in enhancing the energy storage performance.[32,34]

However, LDHs still struggle to realize their theoretical capacity due to agglomeration issues.[35,36] To overcome this weakness, the construction of a rational architecture of the electrode material is one of the most effective strategies. Developing a 3D hierarchical structure in a core–shell form can provide not only a great number of redox-active sites through the enlarged surface area, but also ensure efficient transport pathways for the electrolyte to enhance the ion transport rate. Generally, one-dimensional (1D) core structures such as nanotubes, nanowires, and nanorods offer continuous and undisturbed conduction paths and represent efficient platforms for electron transfer. In the form of interconnected 3D networks, 1D nanostructures offer increased robustness as a support layer,[37] combining high electrical conductivity and enhanced mechanical robustness with an open-porous platform offering efficient paths for both mass and charge transfer, enhancing the kinetics of the redox reactions occurring on the NiCo-LDH surface.[35,38] Meanwhile, two-dimensional (2D) nanosheets are employed as a shell with a large surface area. Such a combination of different dimensionalities brings a supportive effect of the two components, which in turn is reflected in the enhanced energy storage. Moreover, the direct growth of the active material (NiCo-LDH) over the interconnected Ni-network core can hasten the charge transfer rate because of the high conductivity of the Ni core and the strong connection between the active material and the substrate which acts as a current collector without using any binders or conductive agents.[35] Compared to bulk materials, hierarchical nanostructures offer synergetic effects from individual counterparts at the multi-level architecture.[39] Several free-standing NiCo-LDH-based electrodes have been reported in different forms including nanowires, nanosheets, and microflowers and demonstrated high electrochemical performance because of the direct contact with the current collector.[36,40,41] Nevertheless, the dimensions of the electrode are commonly defined by the dimensions of standard substrates including felt, foams, cloths, and 3D-printed materials, which have a large thickness. Consequently, most of these electrodes can achieve high gravimetric capacities but limited volumetric capacity and energy density, which is crucial for portable and wearable devices. While nanotube network structures share general features with conventional conductive substrates (both constitute 3D highly porous interconnected frameworks composed of conductive materials), structural differences include the hollow nature of nanotubes and their straight orientation. The most striking difference, though, is their nanoscale. Accordingly, a suitable fabrication strategy is pivotal for realizing a device that fulfills these requirements in a cost-effective way. Tailoring a hierarchical structure at the nanoscale accompanied by decoration with an electroactive material can address different functionality aspects including high diffusion rates through these nanoreactors.[35,42,43]

Herein, inspired by the natural world, we demonstrate a new feasible strategy to fabricate a stand-alone hierarchical NiCo-LDH@Ni-NTNW heterostructure that imitates the structure of the pipe cactus plant as a new generation of ultrathin electrodes for HSCs that resolves the above issues (Scheme 1). Our approach employs facile and tunable methods for electrode fabrication, namely electroless plating for synthesizing the Ni-NTNW core, and electrodeposition for decorating the nanostructured electrode network with a shell of electroactive NiCo-LDH nanosheets. The proposed strategy is based on scalable and cost-effective techniques which can be adopted for developing different nanotube-based architectures. The as-prepared battery-type NiCo-LDH@Ni-NTNW electrode was encompassed with activated carbon (AC) in a HSC device with outstanding performance. In turn, the assembled device demonstrated high volumetric capacitance, high rate capability, and excellent cycling stability. More importantly, it delivers an ultrahigh volumetric energy density of 14.7 mWh cm^{-3}. The introduced fabrication approach holds important promise in realizing a new generation of ultrathin electrodes with high volumetric energy density for practical applications.

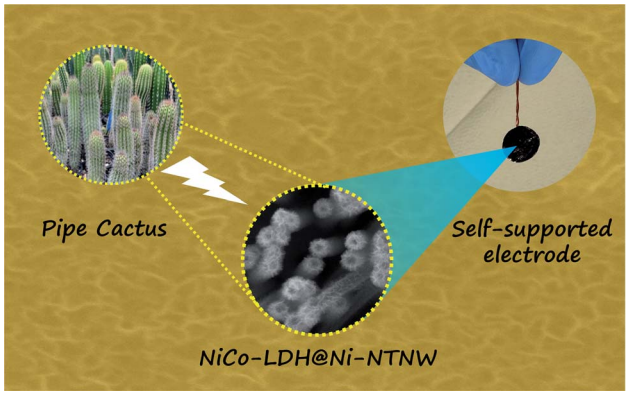

Scheme 1 Pipe cactus-inspired design philosophy of the NiCo-LDH@Ni-NTNW self-supported electrode.

2 Experimental section

2.1 Materials

Polycarbonate membranes (Whatman, nominal thickness 20 μm) with a nominal pore diameter of 200 nm and a pore density of 5×10^8 cm^{-2}. Nickel sulfate heptahydrate ($NiSO_4 \cdot 7H_2O$, purum p.a. cryst., Sigma-Aldrich), borane dimethylamine complex ($(CH_3)_2NH \cdot BH_3$, 97%, Sigma-Aldrich), potassium chloride (KCl, ≥99.0%, Sigma), dichloromethane (CH_2Cl_2, puriss. p.a., Sigma-Aldrich), potassium hydroxide (KOH, Sigma-Aldrich), boric acid (H_3BO_3, 99.5%, Sigma), nickel nitrate hexahydrate ($Ni(NO_3)_2 \cdot 6H_2O$, GR, Merck), cobalt nitrate hexahydrate ($Co(NO_3)_2 \cdot 6H_2O$, 99+%, Acros Organics), palladium chloride ($PdCl_2$, 99.9% metal basis, Alfa Aesar), trifluoroacetic acid (TFA) (CF_3COOH, ≥99.9%, Carl Roth), trisodium citrate dihydrate ($HOC(COONa)(CH_2COONa)_2 \cdot 2H_2O$, puriss. p.a., Sigma-Aldrich), methanol (CH_3OH, 99.5%, AppliChem Panreac), activated carbon (AC) YP-80f (Kuraray Europe GmbH, Finland), polytetrafluorethylene (PTFE, 60 wt% dispersion in H_2O, Sigma-Aldrich), and carbon black (CB) (Imerys, C-NERGY™ SUPER C65). All chemicals were used as received without any further purification. Deionized H_2O (Milli Q, >18 MΩ cm) was used in all processes.

2.2 Fabrication of the self-supported Ni-NTNW electrode

The Ni-NTNW self-supported electrode was prepared *via* template-assisted electroless plating (EP), followed by electrodeposition.[35] Briefly, ion track-etched polycarbonate membranes were exposed to three successive runs of sensitization and activation for 30 and 4 min, respectively. The templates were first soaked in a sensitization bath (42 mM $SnCl_2$ and 71.4 mM TFA in ethanol) and then transferred to an activation bath (11.3 mM $PdCl_2$ and 33.9 mM KCl). In the Pd solution, the templates turn brown, indicating the deposition of Pd nanoparticles. After washing, the activated templates were immersed in an EP bath which contains 100 mM $NiSO_4 \cdot 7H_2O$, 100 mM trisodium citrate dihydrate, and 100 mM borane dimethylamine for around 40 min until a shiny layer of Ni appeared on the outer surface of the template. After the electroless plating, the templates were thoroughly washed with water.

In order to reinforce one side of the template with a supporting layer of Ni, electrodeposition was employed using a Ni electrolyte containing 0.5 M $NiSO_4 \cdot 7H_2O$ and 0.5 M H_3BO_3 and applying a constant potential of −1 V *vs.* Ag|AgCl. Afterwards, the thin Ni surface layer on the other side stemming from EP was removed *via* swapping with aqua regia. Finally, the polymer matrix was dissolved with dichloromethane to achieve full exposure of the NTNW and obtain a self-supported Ni-NTNW electrode.

2.3 Growth of NiCo-LDH nanosheets over Ni-NTNW electrodes

A hierarchical NiCo-LDH@Ni-NTNW electrode was prepared by further electrodeposition of NiCo-LDH nanosheets onto the Ni-NTNW parent electrode. Pulsed electrodeposition was employed using a 1 : 1 molar mixture containing 0.05 M $Co(NO_3)_2 \cdot 6H_2O$ and 0.05 M $Ni(NO_3)_2 \cdot 6H_2O$ as an electrolyte and applying −1 V *vs.* Ag|AgCl for 120 s separated by pulses of +1 V *vs.* Ag|AgCl for 0.5 s every 3 s. Finally, the samples were thoroughly washed with water.

The mass of Ni-NTNW and NiCo-LDH nanosheets was estimated by weighing the template after each step of the preparation procedure. The average mass loadings (estimated from the different samples) of the Ni-NTNW and NiCo-LDH nanosheets were 1.87 and 0.42 mg cm^{-2}, respectively.

2.4 Fabrication of the NiCo-LDH@Ni-NTNW//AC HSC

The HSC was assembled in a two-electrode Swagelok®-cell. The HSC was packed in a sealed assembly by face-to-face sandwiching the hierarchical NiCo-LDH@Ni-NTNW as a positive electrode and self-standing AC sheet (90 wt% AC, 5 wt% CB, 5 wt% PTFE) as a negative electrode, separated by filter paper (EDLC 20–30 TC from SWM company) soaked in 1 M KOH. The mass of NiCo-LDH@Ni-NTNW (m^+) and AC (m^-) electrodes was balanced based on the charge balance according to the following equations:[44]

$$q^+ = q^- \quad (1)$$

$$C^+ m^+ \Delta V^+ = C^- m^- \Delta V^- \quad (2)$$

where C^+ and C^- represent the specific capacitance of NiCo-LDH@Ni-NTNW and the AC, respectively, and ΔV^+ and ΔV^- stand for the potential window of NiCo-LDH@Ni-NTNW and AC electrodes, respectively. The average total mass of the positive (NiCo-LDH layer) and negative (AC sheet) electrodes was calculated to be about 4.6 mg. The overall thickness of the NiCo-LDH@Ni-NTNW//AC HSC including the two electrodes and the separator was calculated to be about 90 μm (20 μm NTNW + ∼30 μm filter paper + ∼40 μm AC).

2.5 Material characterization

Scanning electron microscopy (SEM) was performed by using a Philips XL30 FEG with acceleration voltages of 10–30 kV. X-ray diffraction (XRD) measurements were conducted using a Seifert PTS 3003 diffractometer equipped with a Cu anode in Bragg–Brentano geometry, an X-ray mirror built-in on the primary side, and a long Soller-slit and graphite monochromator on the secondary side to separate the Cu Kα-line (40 kV/40 mA). Raman spectra were obtained by using a Horiba LabRam HR 800 Raman spectrometer with an excitation light of ∼514 nm. Transmission electron microscopy (TEM) micrographs were collected using an FEI CM20 (LaB_6 cathode, 200 kV acceleration voltage) accompanied by an energy dispersive X-ray analysis (EDX) unit.

2.6 Electrochemical experiments

The electrodeposition of the Ni supporting layer was performed in a three-electrode setup containing a circular piece (12 mm diameter) of the electroless plated polymer membranes as the working electrode; Ag|AgCl as the reference electrode; and a Pt

spiral wire as the counter electrode using a Keithley 2602 System SourceMeter unit. The electrodeposition of NiCo-LDH nanosheets was achieved using the previously prepared Ni-NTNW as the working electrode under the same conditions.

The electrochemical experiments were conducted using an OctoStat5000 (Ivium Technologies) electrochemical workstation and Gamry Reference 600 potentiostat. For electrochemical characterization of Ni-NTNW and NiCo-LDH@Ni-NTNW electrodes including cyclic voltammetry (CV), galvanostatic charge–discharge (GCD), and electrochemical impedance spectroscopy (EIS) measurements, a typical three-electrode setup was employed using a Pt spiral wire as a counter electrode, Hg|HgO filled with 1 M KOH as a reference electrode (140 mV *versus* the standard hydrogen electrode), and a circular self-supported NTNW (11 mm diameter after insulating the backside), connected to a Cu wire, as a working electrode. 1 M KOH was used as an electrolyte throughout all measurements. CV was performed in a potential window between 0 and 0.6 V (*vs.* Hg|HgO), and GCD was performed between 0 and 0.5 V (*vs.* Hg|HgO). EIS was conducted at the open circuit potential in the frequency range between 0.01 Hz and 100 kHz combined with a 10 mV disturbance signal.

The gravimetric, areal, and volumetric capacities of the electrodes in the three-electrode cell were estimated from the CV curves according to the following formulae[45]

$$q_m = \frac{1}{2\times\nu\times m}\int I\mathrm{d}V \text{ or } q_a = \frac{1}{2\times\nu\times A}\int I\mathrm{d}V \text{ or } q_d = \frac{1}{2\times\nu\times d}\int I\mathrm{d}V \quad (3)$$

where q_m (C g^{-1}) is the gravimetric capacity, q_a (C cm^{-2}) is the areal capacity, q_d (C cm^{-3}) is the volumetric capacity, $\int I\mathrm{d}V$ represents the integrated area of the entire CV curve, m (g), A (cm^2), and d (cm^3) are the mass, area, and volume of the active material, respectively, and ν (V s^{-1}) is the scan rate.

They were also calculated from the GCV curves according to the following equation:[46]

$$q_m = \frac{I\times\Delta t}{m} \text{ or } q_a = \frac{I\times\Delta t}{A} \text{ or } q_d = \frac{I\times\Delta t}{d} \quad (4)$$

where I (A) represents the discharge current, and Δt (s) is the discharge time.

The gravimetric, areal, and volumetric capacitances, energy density, and power density of the active materials in the two-electrode setup were calculated using the stepwise integration of the following equation:[47,48]

$$C_m = \frac{I}{m}\int\frac{1}{V}\mathrm{d}t \text{ or } C_a = \frac{I}{A}\int\frac{1}{V}\mathrm{d}t \text{ or } C_d = \frac{I}{d}\int\frac{1}{V}\mathrm{d}t \quad (5)$$

$$E_m = \frac{I}{m\times 3.6}\int V\mathrm{d}t \text{ or } E_a = \frac{I}{A\times 3600}\int V\mathrm{d}t \text{ or } E_d = \frac{I}{d\times 3600}\int V\mathrm{d}t \quad (6)$$

$$P = \frac{E\times 3600}{\Delta t} \quad (7)$$

where C_m (F g^{-1}) is the gravimetric capacitance, C_a (F cm^{-2}) is the areal capacitance, and C_d (F cm^{-3}) is the volumetric capacitance. C_d of the HSC device was estimated using the total thickness of the HCS including the AC and the separator, not only the thickness of the electrode. E_m (Wh kg^{-1}) is the gravimetric energy density, E_a (Wh cm^{-2}) is the areal energy density, E_d (Wh cm^{-3}) is the volumetric energy density, and P is the power density (*i.e.*, gravimetric, areal, or volumetric power density).

3 Results and discussion

Our 3D-NTNW is characterized by interconnected dense arrays of nanotubes replicating the initial density and intersections of the nanochannels in the used ion track-etched polycarbonate membranes. The process of Ni electroless plating demands a large enough areal density of metal seeds uniformly distributed over the inner surface of the template pores to initiate the autocatalytic Ni-plating process and obtain continuous and homogeneous deposition on the inner template surfaces. The seeding process includes sensitization and activation of the templates, where Sn^{2+} ions are electrostatically attached to the polymer template surface from the sensitization bath and employed to reduce the Pd^{2+} ions from the activation bath forming metallic Pd nanoparticles which are adsorbed on the template surface and act as seeds for the later plating process.[49] Electroless plating was employed as a simple technique to grow a uniform layer of Ni nanoparticles inside the seeded pores and over the outer surface. The plating process is accompanied by hydrogen evolution which decreases gradually with the decrease of the deposition rate until a shiny film of Ni completely covers the template and blocks access to the inner surface of the pores as indicated in the first step in Fig. 1.

A new approach has been developed *via* hierarchical functionalization to achieve a flexible paradigm of free-standing electrodes that can be adopted to decorate the NTNW with different active materials for different applications. In order to fabricate such a free-standing nanostructured electrode, the Ni-NTNW was reinforced with a back layer of Ni to work as a mechanically robust layer that carries the Ni-NTNW and can be easily connected to a potentiostat using a copper wire. Electrodeposition was employed to form a uniform layer of Ni over one side of the electroless-plated membrane forming a silver shiny layer of Ni supporting layer (step 2 in Fig. 1). Such an approach offers a robust integrated design of the electrode that enhances the conductivity and can be easily handled without damage. Afterwards, the thin surface layer plated on the other side during the electroless plating step was chemically etched (step 3 in Fig. 1) to fully expose the Ni-NTNW and facilitate the dissolution of the polymer matrix using dichloromethane, which in turn enhances the accessibility of the electrolyte to the active sites of the Ni-NTNW. As a result, only the central supported area remained intact while the surrounding area of the NTNW was separated (step 4 in Fig. 1).

The Ni-NTNW was further decorated with NiCo-LDH nanosheets *via* pulsed electrodeposition to obtain a modified NiCo-LDH@Ni-NTNW core–shell nanostructure (step 5 in Fig. 1).

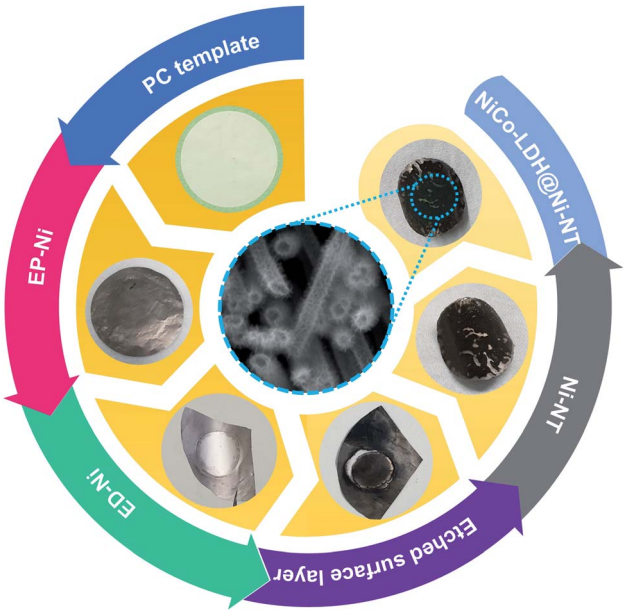

Fig. 1 Schematic illustration presenting photographs of the self-supported NiCo-LDH@Ni-NTNW electrode through the fabrication process. After electroless plating of Ni (step 1), electrodeposition is conducted (step 2) to get a thicker supporting layer of Ni on one side of the template (the bright round area in the sample center). In step 3, the other side of the sample is chemically etched to eliminate the electroless deposited surface layer, followed by dissolution of the polymer matrix to isolate the Ni-NTNW (step 4). The final NiCo-LDH@Ni-NTNW electrode is obtained by electrodeposition of LDH (step 5).

The single-step electrodeposition of NiCo-LDH includes the electrochemical reduction of nitrate ions and the consequent production of hydroxyl ions which afterward react with the existing Ni^{2+} and Co^{2+} ions in the electrolyte forming NiCo-LDH nanoflakes over Ni-NTNW.[50] The as-prepared NiCo-LDH@Ni-NTNW acts as a self-supported electrode where NiCo-LDH nanosheets are grown over the interconnected Ni nanotube array which keeps the whole structure attached to the back supporting layer. Such a well-designed electrode architecture comprises a 3D interconnected porous network that enables high accessibility of the electrolyte and a highly conductive metal core that accelerates the electron transfer acting as a binder-free current collector. Meanwhile, the NiCo-LDH nanosheets offer numerous electroactive sites.

The morphology of the nanostructured integrated electrode was explored using SEM (Fig. 2). The top view of the pristine Ni-NTNW (Fig. 2a and b) shows uniform nanotubes with a diameter of around 200 nm reflecting the original diameter of the nanopores in the used polycarbonate templates. The lateral view of Ni-NTNW (Fig. 2c) confirms the conformal deposition during the electroless Ni plating, resulting in intact and homogeneous Ni nanotubes replicating the whole pores of the parent templates. This nanotube array has a free-standing interconnected structure (Fig. 2c) due to the frequent intersections between the tubes, forming a highly conductive 3D metallic core which in turn acts as an efficient current collector.

As for the NiCo-LDH@Ni-NTNW electrode displayed in Fig. 2d and e, the NiCo-LDH nanosheets covering the Ni-NTNW skeleton can be easily distinguished due to their wrinkled structure. As result, a core–shell architecture is obtained in which the NiCo-LDH nanosheets evenly cover the nanotube support while still maintaining the features of the Ni-NTNW backbone. This structural motif is characterized by a firm connection of the nanosheets to the metal core and the homogeneous covering across the whole surface of the Ni-NTNW, providing good mechanical and electrical contact (Fig. 2f). The employed deposition time represents a compromise between a high amount of NiCo-LDH as redox-active material to boost the energy density while keeping the porous structure of the catalyst with its torturous pathways free from clogging,[35] which facilitates the accessibility of the electrolyte to the active sites on the tubes, resulting in a great contribution to the reversible and fast faradaic reactions and an enhanced capacity of the electrode.[51,52] The successful incorporation of NiCo-LDH was further confirmed by EDX measurements performed on the large area lateral view of the as-prepared Ni-NTNW and NiCo-LDH@Ni-NTNW as shown in Fig. 2c and f, respectively. The EDX spectrum of Ni-NTNW shows only the peaks of Ni which are assigned to Ni-Kα and Ni-Kβ at ~7.4 and 8.2 keV, respectively,[53] while that of NiCo-LDH@Ni-NTNW shows an additional characteristic peak for Co which is assigned to Co-Kα at ~6.9 keV besides the Ni peaks, confirming the presence of Ni as well as Co content. These findings are consistent with the SEM observations and further confirm the successful deposition of NiCo-LDH nanosheets on the Ni-NTNW core structure. From the EDX spectrum of the NiCo-LDH@Ni-NTNW, the atomic ratio of Ni : Co is 41 : 12, and the mass ratio is 59 : 17. The atomic ratio of Ni is higher than that of Co due to the great contribution of the Ni-NTNW as the percentage of the NiCo-LDH represents around 18% of the NiCo LDH@Ni-NTNW total mass.

The crystalline structure of Ni-NTNW and NiCo-LDH@Ni-NTNW was investigated using XRD. As represented in Fig. 3a, both electrode materials display intense and sharp diffraction peaks at 44.4°, 51.9°, and 76.3° which well correspond to the (111), (200), and (220) crystalline planes of face-centered cubic Ni, respectively.[35] These peaks can be assigned to the metallic Ni-NTNW core. The broad diffraction peak in between 15 and 35° can be assigned to the used glass.[54] As we can see in the XRD pattern of NiCo-LDH@Ni-NTNW, some new wide characteristic peaks appear (distinguished with a black label) which match well with the hydrotalcite-like NiCo-LDH phase (JCPDS 40-0216), confirming that NiCo-LDH has been successfully grown over the nanotube network.[55,56] The reflexes of this hydrotalcite-like structure have weak intensities (compared to those of the metallic Ni core) due to the weak crystallinity and ultrathin structure of the NiCo-LDH nanosheets.[35] Raman spectroscopy was employed to assure the loading of NiCo-LDH and investigate the chemical structure of NiCo-LDH@Ni-NTNW (Fig. 3b). The spectrum shows two characteristic peaks at 461 and 527 cm^{-1}, which can be assigned to the vibrational modes of Ni–O and Co–O, confirming the findings from the XRD measurement.[57,58]

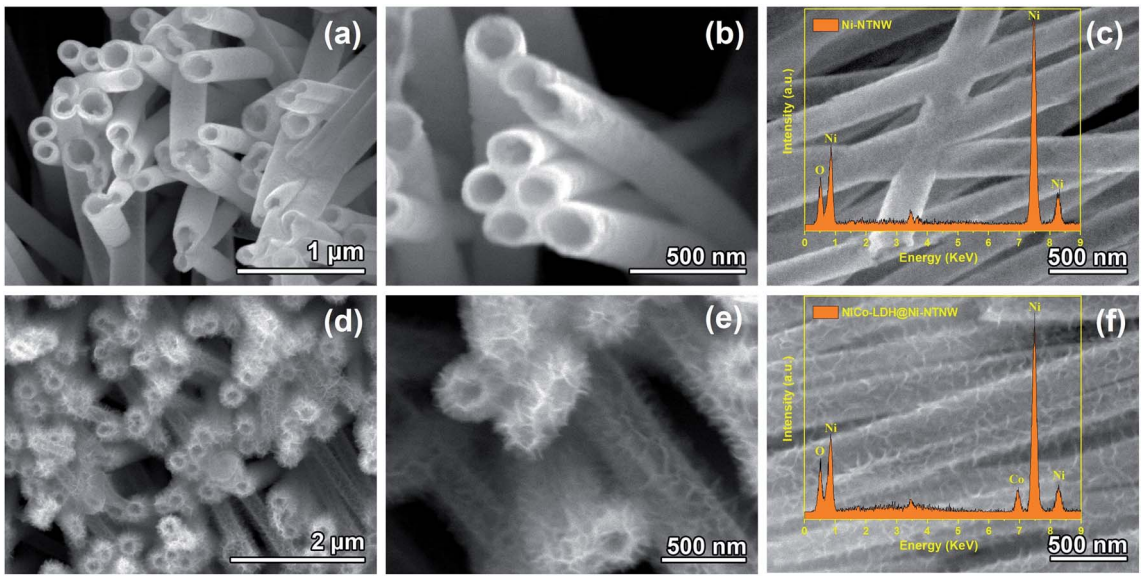

Fig. 2 SEM top view of Ni-NTNW (a and b) and NiCo-LDH@Ni-NTNW (d and e). SEM lateral view with EDX spectra of Ni-NTNW (c) and NiCo-LDH@Ni-NTNW (f).

The hierarchical structure of the as-prepared electrode has been explored by TEM accompanied by EDX. Fig. 3c shows the TEM micrograph of NiCo-LDH@Ni-NTNW, in which the core Ni network appears darker than the surrounding NiCo-LDH shell. The Ni-NTNW is composed of fine nanoparticles which are reflected in the homogeneous and uniform structure of the tubes

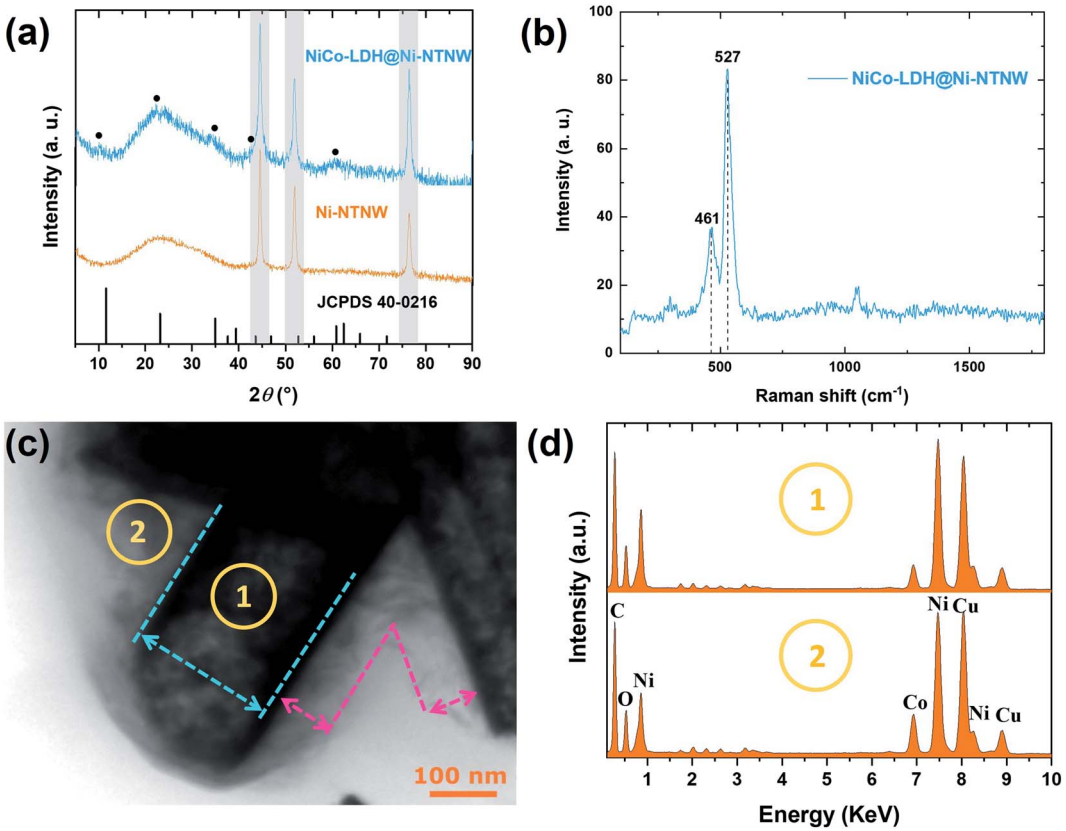

Fig. 3 (a) XRD patterns of Ni-NTNW and NiCo-LDH@Ni-NTNW, and the reference peaks of the JCPDS file No. 40-0216. (b) Raman spectrum of NiCo-LDH@Ni-NTNW, (c) TEM lateral view of NiCo-LDH@Ni-NTNW with a dashed turquoise line representing the borders of the core Ni-NTNW and dashed rose color representing the surrounding NiCo-LDH shell, and (d) EDX spectra at two different spots in the TEM micrograph representing the center of the tube (position 1) and the center of NiCo-LDH coating nanosheets (position 2).

without any gaps. The deposition of the NiCo-LDH nanosheets with their flaky morphology can be observed covering the Ni-NTNW from all sides. Elemental analysis was conducted for the core and shell of the NiCo-LDH@Ni-NTNW composite (distinguished by positions 1 and 2, in Fig. 3c, respectively) and the corresponding spot EDX spectra are represented in Fig. 3d. As can be seen, the spectrum collected at the surrounding shell at position 2, which contains the NiCo-LDH nanosheets, reveals a higher Co-to-Ni ratio compared to the center of the Ni-NTNW (position 1), which is attributed to the contribution of the additional Ni content from the walls of the core nanotubes under the covering NiCo-LDH sheets. The EDX spectra confirm the well-defined hierarchical structure of the NiCo-LDH@Ni-NTNW electrode with homogeneous distribution of the LDH on the core Ni tubes, which is consistent with the findings from the SEM, XRD, and Raman measurements.

To evaluate the electrochemical performance of the as-prepared Ni-NTNW and NiCo-LDH@Ni-NTNW composites as efficient positive electrodes for HSC, different electrochemical techniques including CV, GCD, and EIS have been employed as represented in Fig. 4. A three-electrode cell was used to monitor the behavior of the self-supported electrodes. As shown in Fig. 4a, the prepared electrodes which are soldered to a Cu wire are directly soaked in the electrolyte solution and can be easily connected to the potentiostat without any need for binders or supporting electrodes, which are commonly used to carry the active material. CV curves of the Ni-NTNW and NiCo-LDH@Ni-NTNW electrodes were recorded in the potential window between 0 and 0.6 V (*vs.* Hg/HgO) at a scan rate of 10 mV s^{-1}, indicating a typical battery-like behavior with pairs of distinct redox peaks that originate from the faradaic reactions of OH^- ions with $Ni(OH)_2$ in the case of the Ni-NTNW electrode and with $Ni(OH)_2$ and $Co(OH)_2$ in the case of the NiCo-LDH@Ni-NTNW electrode (Fig. 4b). The displayed peak pair of Ni-NTNW can be corresponded to the Ni^{2+}/Ni^{3+} conversion, while NiCo-LDH@Ni-NTNW exhibits two oxidation peaks corresponding to Co^{2+}/Co^{3+} and Co^{3+}/Co^{+4} conversions according to the following equations:[5,35]

$$Ni(OH)_2 + OH^- \rightarrow NiO(OH) + H_2O + e^- \quad (8)$$

$$Co(OH)_2 + OH^- \rightarrow CoO(OH) + H_2O + e^- \quad (9)$$

$$CoO(OH) + OH^- \rightarrow CoO_2 + H_2O + e^- \quad (10)$$

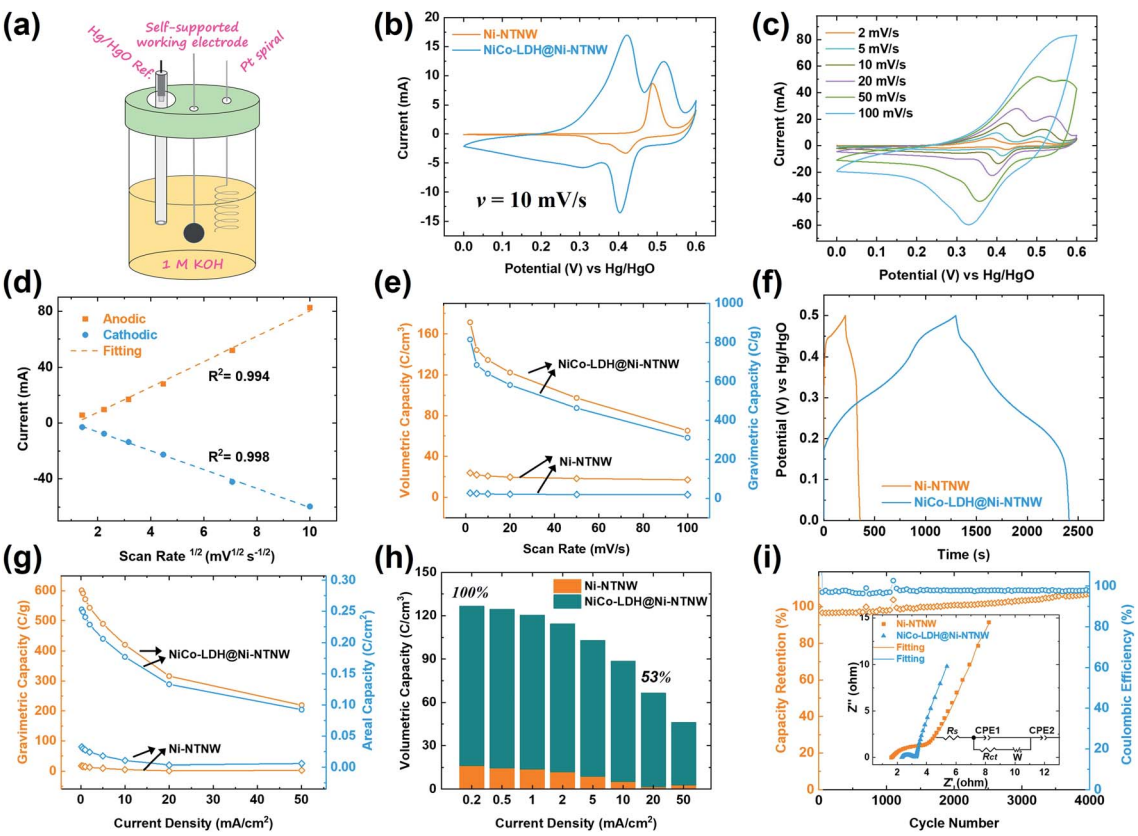

Fig. 4 (a) Schematic illustration of the three-electrode cell employed for electrochemical evaluation. (b) CV of Ni-NTNW and NiCo-LDH@Ni-NTNW electrodes at 10 mV s^{-1} (c) CV curves obtained at different scan rates between 2 and 100 mV s^{-1} and (d) the corresponding oxidation and reduction peak currents as a function of $\nu^{1/2}$ of the NiCo-LDH@Ni-NTNW electrode. (e) Volumetric and gravimetric capacities of Ni-NTNW and NiCo-LDH@Ni-NTNW electrodes estimated from the CV curves at different scan rates. (f) GCD curves of Ni-NTNW and NiCo-LDH@Ni-NTNW electrodes at 0.2 mA cm^{-2}. (g) Gravimetric and areal capacities and (h) volumetric capacities of Ni-NTNW and NiCo-LDH@Ni-NTNW electrodes estimated from the GCD curves at different current densities. (i) Cycling stability of the NiCo-LDH@Ni-NTNW electrode at a current density of 20 mA cm^{-2} (inset: EIS plots of both electrodes and the corresponding equivalent circuit).

It is apparent in Fig. 4b that the NiCo-LDH@Ni-NTNW electrode demonstrates much larger peak current densities and greater integrated area under the CV curves compared to the Ni-NTNW electrode, indicating enhanced electrochemical activity and higher storage capacity, albeit the surface of the Ni backbone itself also contributes to the redox activity to a minor extent. Comparison of the CV curves of both electrodes at different scan rates, namely 20 and 50 mV s^{-1}, demonstrated the same behavior as shown in Fig. S1,† confirming the enhanced capacity offered by the NiCo-LDH@Ni-NTNW electrode. This can be attributed to the larger surface area introduced upon decorating the core Ni nanotubes with the NiCo hydroxide layer which in turn is reflected in the number of the available active sites on the surface and the better exposure to the electrolyte. Moreover, the reversibility of the NiCo-LDH@Ni-NTNW electrode was enhanced due to the Co doping, which is vital for improving the coulombic efficiency and utilization of the electrode. CV curves of the NiCo-LDH@Ni-NTNW electrode were recorded within the potential window of 0–0.6 V (*vs.* Hg/HgO) at different scan rates between 2 and 100 mV s^{-1} (Fig. 4c), and the redox peaks at different scan rates confirmed the same battery-like behavior of the electrode with a clear increase in the peak current and a shift in the positive and negative directions for the anodic and cathodic peaks, respectively, upon increasing the scan rate due to the internal resistance of the electrode or polarization.[59] As can be seen in Fig. 4c, the NiCo-LDH@Ni-NTNW electrode shows clear redox peaks at different scan rates because of the rapid electron transfer through the hierarchical structure which is confirmed by the linear fitting of the peak current *vs.* the square root of the scan rate (Fig. 4d). For comparison, the cyclic voltammograms were recorded for the Ni-NTNW electrode at the same scan rates (Fig. S2†) and revealed the same battery-like behavior at all scan rates with good electrochemical reversibility which is further evidenced by the direct proportion between the peak currents and the square root of the scan rate (Fig. S3†). The volumetric and gravimetric capacities of both electrodes (Fig. 4e) have been estimated from the corresponding CV curves at different scan rates. There is a slight change between the capacities estimated from the CV curves and those calculated from GCD measurements because the accumulated area under the CV curves includes a small contribution from the oxygen evolution reaction which results in higher capacities. The NiCo-LDH@Ni-NTNW electrode showed much higher volumetric and gravimetric capacities compared to the Ni-NTNW electrode at all scan rates as seen in Fig. 4e. It is worth mentioning that the main advantage of our electrode design is its ultrathin thickness (20 μm) imitating the thickness of the parent template as shown in the cross-sectional micrograph of the electrode (Fig. S4†), which is clearly reflected in its exceptional volumetric capacity. At 2 mV s^{-1}, the NiCo-LDH@Ni-NTNW electrode revealed a capacity of 171 C cm^{-3} which is about 7 times as much as the corresponding value of Ni-NTNW (23.7 C cm^{-3}). Moreover, at a high scan rate of 50 mV s^{-1}, the NiCo-LDH@Ni-NTNW electrode still retains a high capacity of 97.4 C cm^{-3} which represents around 56% of that at 2 mV s^{-1} for the same electrode. The demonstrated huge volumetric capacity opens the door for this ultrathin hierarchical design to be used in different applications which have dimensional limitations such as portable electronics and wearable devices. Moreover, the thickness of the NTNW could be controlled to boost the capacity. Larger thicknesses up to about 60 μm can be realized with ion track etching or through the preparation of bulky nanowire aerogels.[60,61] The NiCo-LDH@Ni-NTNW electrode exhibited much higher gravimetric capacity (Fig. 4e) and areal capacity (Fig. S5†) in comparison with the Ni-NTNW electrode at all scan rates. These findings prove that the capacitive properties are significantly improved *via* the synergistic effect of the decoration with NiCo-LDH nanosheets.

GCD measurements for Ni-NTNW and NiCo-LDH@Ni-NTNW electrodes were conducted between 0 and 0.5 V (*vs.* Hg/HgO) at different current densities ranging from 0.2 to 50 mA cm^{-2} (Fig. S6 and S7,† respectively). The GCD curves of both electrodes reveal nonlinear charge and discharge behaviors at all current densities, implying that the dominant capacitive behavior is of the battery type which is consistent with the results from CV measurements and the literature-known properties of redox-active Ni LDHs.[36,40] It is also clear in the GCD curves of both electrodes that they have approximately similar charge and discharge times which in turn indicates high coulombic efficiency and thus that the charge–discharge process is reversible.[40] GCD processes of Ni-NTNW and NiCo-LDH@Ni-NTNW electrodes at a current density of 0.2 mA cm^{-2} are represented in Fig. 4f, and as shown, the NiCo-LDH@Ni-NTNW electrode demonstrates a much longer discharge time (1116 s) compared to the Ni-NTNW (147 s), which reflects the higher capacity offered by this improved electrode design. The same discharge behavior was observed at a current density of 0.5 mA cm^{-2} (Fig. S8†). The areal and gravimetric specific capacities (Fig. 4g) were obtained from the discharge part of the GCD curves of Ni-NTNW (Fig. S6†) and NiCo-LDH@Ni-NTNW (Fig. S7†) electrodes at different current densities. The gravimetric and areal capacities of NiCo-LDH@Ni-NTNW at a current density of 0.2 mA cm^{-2} reached 601.1 C g^{-1} (=1202.2 F g^{-1}) and 0.25 C cm^{-2}, respectively, compared to 17.3 C g^{-1} and 0.032 C cm^{-2} for Ni-NTNW at the same current density. The calculated gravimetric and areal capacities of Ni-NTNW are much lower and incomparable to those of NiCo-LDH@Ni-NTNW at all current densities. More importantly, the NiCo-LDH@Ni-NTNW electrode was able to offer a superior volumetric capacity which can be attributed to the thin-layered hierarchical structure (20 μm) enriched with active sites and the enhanced charge transfer due to the improved electrical conductivity arising from valence interchange or charge hopping between the Ni and Co cations.[62] As displayed in Fig. 4h, the NiCo-LDH@Ni-NTNW electrode achieved a high capacity of 66 C cm^{-3} (=132 F cm^{-3}) at a high current density of 20 mA cm^{-2}, retaining 53% of its initial capacity at 0.2 mA cm^{-2} (126.4 C cm^{-3}, corresponding to 252.8 F cm^{-3}), which implies high rate capability. It is important to highlight that the main advantage of our 3D porous architecture is that it offers a much higher interior surface area compared to other substrates such as Ni foams or fibers. This principle is evidenced by the value of volumetric capacity of our NiCo-

LDH@Ni-NTNW electrode which was 2.5-fold that of the NiCo LDH/3D-Ni electrode (13.56 mAh cm^{-3}) at 0.5 mA, which is based on thick Ni wires as a substrate, as recently reported in ref. [63]. The outstanding volumetric capacities of our NiCo-LDH@Ni-NTNW electrode are markedly superior and surpass most of the recently reported NiCo-based battery-type electrodes; moreover, it delivers higher/comparable gravimetric and areal capacities as presented in Table S1.†

Consequently, it is concluded that these remarkable capacitive properties of the NiCo-LDH@Ni-NTNW electrode are linked to the unique hierarchical design of the electrode with its 3D nanostructured core–shell architecture. The electrode kinetics were investigated by EIS measurements for both electrodes. As represented in the inset of Fig. 4i, the Nyquist plot of the NiCo-LDH@Ni-NTNW electrode reveals a semicircle with a smaller diameter compared to Ni-NTNW in the high-frequency region, suggesting a lower charge transfer resistance during the electrochemical reaction due to the inclusion of Co into the NiCo-LDH which leads to the formation of the conductive CoOOH during the discharging process, resulting in the increase of electrode conductivity.[64] Moreover, it shows a slightly steeper line compared to Ni-NTNW in the low-frequency region, indicating a fast ion diffusion process that enhances the capacitive behavior of the electrode.[65] The cycling stability is one of the most important factors for evaluating the overall performance of the electrode in the different applications. The as-prepared NiCo-LDH@Ni-NTNW electrode exhibited outstanding cycling stability. Over the course of 4000 cycles at a current density of 20 mA cm^{-2}, the capacity not only did not decline but even slightly increased to 106%, while the coulombic efficiency fluctuated around 98% (Fig. 4i). This indicates that a small amount of active sites in the 3D porous hierarchical structure are gained after starting the operation of the device, which could be attributed to an electrochemical restructuring of the LDH layer, or superficial oxidation of the Ni nanotubes. This introduced interconnected porous structure can effectively compensate for the volume expansion of electrode materials.[66] Cycling of the Ni-NTNW electrode showed a sudden increase during the first cycles and then gradually decreased (Fig. S9†), which may be attributed to the self-activation of the electrode material that facilitates increased diffusion of the electrolyte into the interior spaces of the Ni network which in turn activates the pseudo-capacitive process.[66,67] Post-analysis of the electrode surfaces confirmed the stability of the electrodes after cycling as demonstrated in the SEM micrographs (Fig. S10†). SEM showed that both the Ni-NTNW and the decorating hydroxide layer remain intact after running the cycling test, and the accompanied EDX spectra confirmed the elemental composition of the electrodes (Fig. S10†). Based on the previously mentioned characteristics and the enhanced performance of the NiCo-LDH@Ni-NTNW electrode, namely high capacity, elevated redox activity, and enhanced cycling stability, the self-supported hierarchical structure is assumed to offer different merits during the electrochemical process including (i) a novel highly porous interconnected structure with a high ion diffusion rate, (ii) efficient metallic pathways through the Ni core that offer high conductivity and fast charge transfer, and (iii) synergy established upon insertion of the LDH shell, enriched with redox-active sites; moreover the combination between Ni and Co can increase the OH^- adsorption energy.[67] These distinguishing characteristics of the NiCo-LDH@Ni-NTNW electrode enable it to serve as an efficient candidate electrode in the HSC.

In order to ensure high-energy storage of the as-prepared NiCo-LDH@Ni-NTNW electrodes in practical applications, a HSC of NiCo-LDH@Ni-NTNW//AC was assembled in a two-electrode system as sketched in Fig. 5a, in which the NiCo-LDH@Ni-NTNW electrode is employed as the positive electrode (battery-type electrode) and AC as the negative electrode (capacitive electrode). Employing the conventional carbonaceous materials with their high surface area in HSCs helps in maintaining satisfactory power density.[47,68] The mass loadings of the two electrodes were adjusted based on the charge balance according to eqn (2) to boost the energy density of the device.[69] The CV curves of the AC electrode were obtained at different scan rates between 2 and 100 mV s^{-1} (Fig. S11†) and revealed the typical rectangular shape of the capacitive electrodes. CV curves of NiCo-LDH@Ni-NTNW and AC electrodes were recorded at a scan rate of 10 mV s^{-1} to determine the optimum operating voltage window of the HSC. As represented in Fig. 5b, the AC electrode demonstrated typical performance of double-layer materials in the potential window between −1 and 0 V (*vs.* Hg/HgO), while the NiCo-LDH@Ni-NTNW electrode showed typical capacitance of the battery-like materials with redox activity in the potential window between 0 and 0.6 V (*vs.* Hg/HgO), delivering a theoretical working voltage around 1.6 V. Fig. 5c demonstrates the CV curves of the hybrid NiCo-LDH@Ni-NTNW//AC device at a scan rate of 10 mV s^{-1} within different voltage windows ranging between 1.2 and 1.8 V. The assembled supercapacitor maintained the same behavior in the CV curves, as the voltage window increased from 1.2 to 1.6 V, without any evidence of oxygen evolution. Further increasing the maximum voltage limit to 1.8 V resulted in oxygen evolution accompanied by a sharp increase in the current density, confirming that the most suitable voltage window for sustained operation of the device without any fluctuations is 0–1.6 V. It can be seen that the areas under the CV curves increase as the voltage window increases, indicating higher capacities.

As shown in Fig. 5d, a mixed behavior of pseudocapacitance and electrical double-layer capacitance is observed in the CV curves of the assembled HSC in the voltage window of 0–1.6 V at different scan rates from 5 to 100 mV s^{-1}, compared to the typical battery-type behavior demonstrated by the CV curves of the NiCo-LDH@Ni-NTNW electrode in the three-electrode system (Fig. 4c), confirming the association of two charge storage mechanisms. The CV curves retained similar shapes with an increased redox peak current and area upon increasing the scan rate, demonstrating fast electron transport and good reversibility.[1] The kinetics of the NiCo-LDH@Ni-NTNW//AC hybrid device was evaluated by analyzing the CV curves at different scan rates. The total measured current (i) can be derivatized using the power law into two components: (1) the current resulting from the diffusion-controlled battery-type process (i_{diff}), and (2) the current resulting from the surface

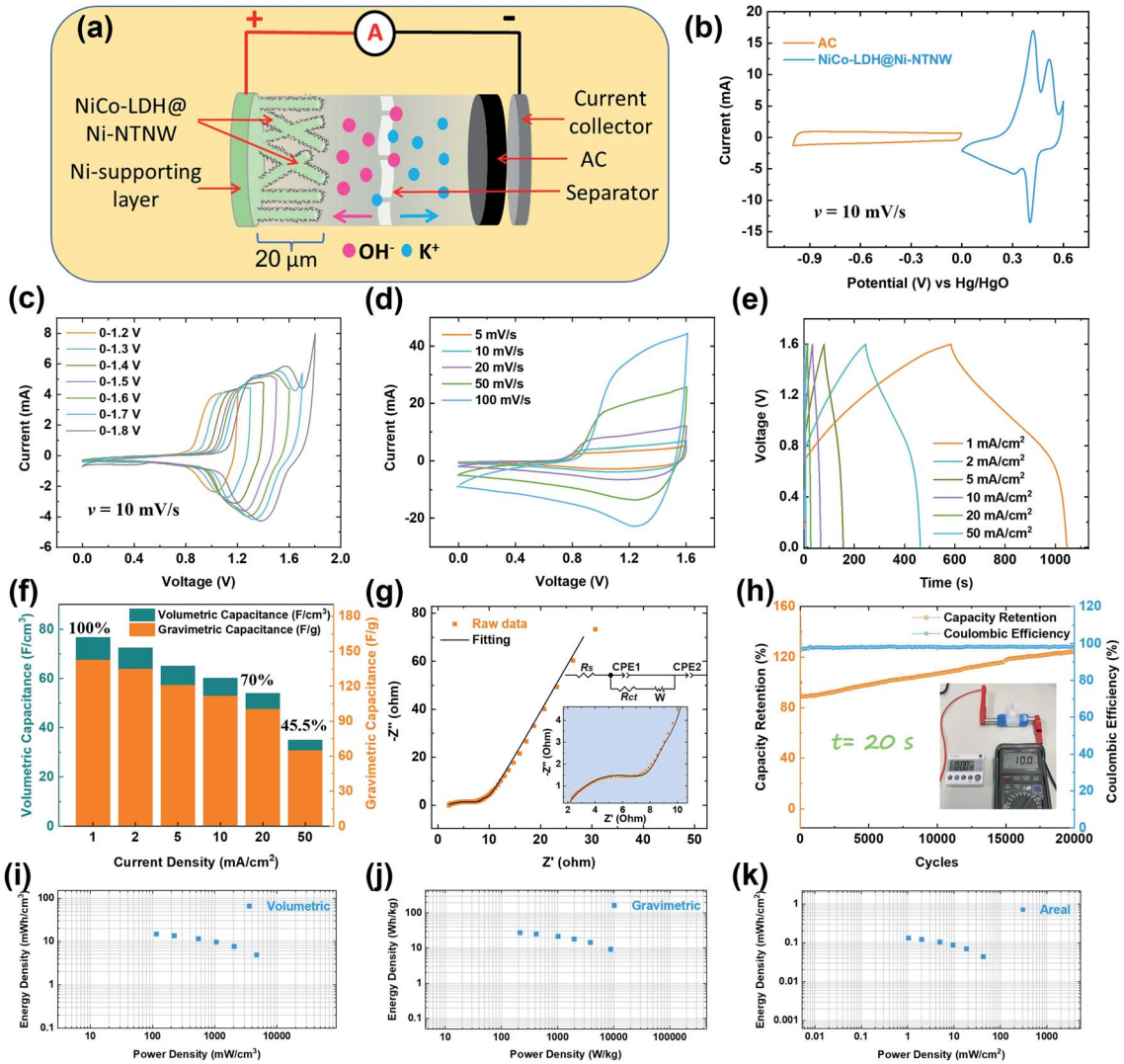

Fig. 5 (a) Schematic illustration of the assembled NiCo-LDH@Ni-NTNW//AC HSC. (b) CV curves of the AC and NiCo-LDH@Ni-NTNW electrodes at 10 mV s^{-1} (c) and (d) CV curves of the HSC in different voltage ranges and at different scan rates, respectively. (e) GCD curves of the HSC at different current densities. (f) Calculated volumetric and gravimetric capacitances of the HSC at different current densities. (g) EIS plot and the corresponding equivalent circuit of the device. (h) Cycling stability of the HSC (inset: image of the assembled device after 20 s of discharging). Ragone plots of (i) volumetric, (j) gravimetric, and (k) areal energy and power densities of the assembled HSC device.

capacitance-dominated process (i_{cap}), according to the following equations:[7]

$$i = av^b \quad (11)$$

$$i = \log a + b \log v \quad (12)$$

where a and b are empirical constants. The ideal behavior either of a diffusion-controlled process or a capacitive-controlled process results in b values of 0.5 and 1.0, respectively.[7,70] The inset of Fig. S12† displays the plots of log I *vs.* log v of the anodic peaks of the CV curves in Fig. 5d at different voltages covering the whole CV curve. The calculated b values varied between 0.7 and 1.0 at all voltages ranging from 0.2 to 1.6 V (except at a voltage of 0.8 V) as shown in Fig. S12,† confirming combined pseudocapacitive diffusion-controlled and double-layer capacitive processes. These mixed charge storage mechanisms play an important role in establishing a device with high capacity, in which the battery-type material offers multiple electrons through the redox reactions, while the double-layer capacitive material assures fast charging through the ionic adsorption.[71]

To investigate the capacitance and evaluate the rate capability of the assembled HSC device, GCD measurements were conducted at different current densities between 1 and 50 mA cm^{-2} (Fig. 5e). The GCD curves in the voltage window of 0–1.6 V revealed symmetric charge and discharge behavior with nearly the same times indicating high coulombic efficiency and reversibility. It is also noticed that the curves followed a non-linear charging and discharging pattern confirming the combined energy storage mechanisms (pseudocapacitive and double-layer capacitive) of both NiCo-LDH@Ni-NTNW and AC

electrodes, which is usually demonstrated by the hybrid devices and in good consistency with the findings from CV analyses.

Based on the GCD tests, the volumetric, gravimetric, and areal capacitances of the as-assembled HSC were calculated, ranging from 34.9–76.7 F cm^{-3} (volumetric) upon increasing the current density from 1 to 50 mA cm^{-2}, which correspond to gravimetric capacitances (calculated based on the total mass of the two electrodes) of 64.9–142.6 F g^{-1} as represented in Fig. 5f. It has to be pointed out that the volumetric capacitance was calculated based on the total volume of the HSC including the two electrodes and the separator. Such high volumetric capacitance (76.7 F cm^{-3} at 1 mA cm^{-2}) significantly surpasses those offered by most of the asymmetric and hybrid devices with high volumetric capacitances including $Co(OH)_2$@CW//CW,[72] Co_9S_8//Co_3O_4@RuO_2,[73] NiCoP/Ti_3C_2 MXene//AC,[74] MnO_2/TCC//TCC[75] and others as reported in Table S2.† Moreover, the device was able to retain high capacitances of 70% and 45.5% even at higher current densities of 20 and 50 mA cm^{-2}, respectively, confirming the excellent rate capability of the HSC device. The areal capacitance of the device is also reported in Fig. S13† and showed the same behavior with 0.7 F cm^{-2} at 1 mA cm^{-2} which dropped to 0.48 F cm^{-2} at 20 mA cm^{-2}. The excellent performance of the NiCo-LDH@Ni-NTNW//AC HSC can be evidenced by the EIS measurement as represented by the Nyquist plot and the corresponding equivalent circuit in Fig. 5g. The device demonstrated low series resistance (R_s) and charge transfer resistance (R_{ct}) of 1.8 and 6.8 Ω, respectively, indicating good charge transfer kinetics of the assembled device.[76,77] The long-term coulombic efficiency and cycling stability are other vital parameters, which determine the suitability of the device for use in practical applications. Hence, the assembled HSC was cycled up to 20 000 cycles at a current density of 20 mA cm^{-2} (Fig. 6h). The device retained around 120% of its initial capacitance. As shown in Fig. 5h, at the beginning of the process, the capacitance increases by around 20% of its initial capacitance, and then it stabilizes during the last 5000 cycles, which may be attributed to the activation of the NiCo-LDH@Ni-NTNW and AC electrodes and the wettability of the interior active sites of NiCo-LDH@Ni-NTNW in the alkaline aqueous media, which in turn get involved in the charging and discharging processes as reported in the previous studies, confirming the superb cycling stability.[78,79] Previous studies showed the same trend of increased capacitance upon cycling. For example, NiCo-LDH/graphene/Ni foam revealed 116% retention after 5000 cycles in a three-electrode setup,[57] NiCo-LDH//graphene revealed 110% retention,[80] and NiCo-LDH//CNT retained 104% of its initial capacitance.[79] However, better stability may be accomplished by prior activation of the device until it reaches a steady state as the capacity increase is mainly focused at the beginning of cycling. Table S3† summarizes the recently reported advanced asymmetric and hybrid supercapacitors with excellent cycling stability. In addition, the coulombic efficiency maintained a high value of around 98% throughout the cycling process, demonstrating the good reversibility of the device. The long-term cycling stability of the HSC device profits from the huge surface area and hierarchical structure of the electrode, which in turn facilitates the diffusion of OH^- ions and provides enough space for buffering the expansions during the charge and discharge processes.[78]

The energy and power densities of the NiCo-LDH@Ni-NTNW//AC HSC were calculated from the measured values of capacitances according to eqn (6) and (7), respectively. The Ragone plots of the device (Fig. 5i–k) present the volumetric, gravimetric, and areal energy densities as a function of the volumetric, gravimetric, and areal power densities, respectively. With a current density of 1 mA cm^{-2}, the HSC delivers a high energy density of 27.5 Wh kg^{-1} (0.13 mWh cm^{-2}) at a power density of 214.7 W kg^{-1} (1.03 mW cm^{-2}). Upon increasing the power density to 8867.5 W kg^{-1} (42.9 mW cm^{-2}), the energy density dropped to 9.1 Wh kg^{-1} (0.04 mWh cm^{-2}) at a higher current density of 50 mA cm^{-2}, indicating the good overall properties of the device. More significantly, our device with its ultrathin structure was able to achieve a remarkable volumetric energy density. It exhibits a volumetric energy density of 14.7 mWh cm^{-3} at a power density of 115.4 mW cm^{-3} with a current density of 1 mA cm^{-2}. Furthermore, with a higher current density of 50 mA cm^{-2}, it retains an energy density of 4.9 mWh cm^{-3} at a higher power density of 4769.3 mW cm^{-3}. The accomplished superior volumetric energy density (14.7 mWh cm^{-3}) outperforms the emerging symmetric, asymmetric, and

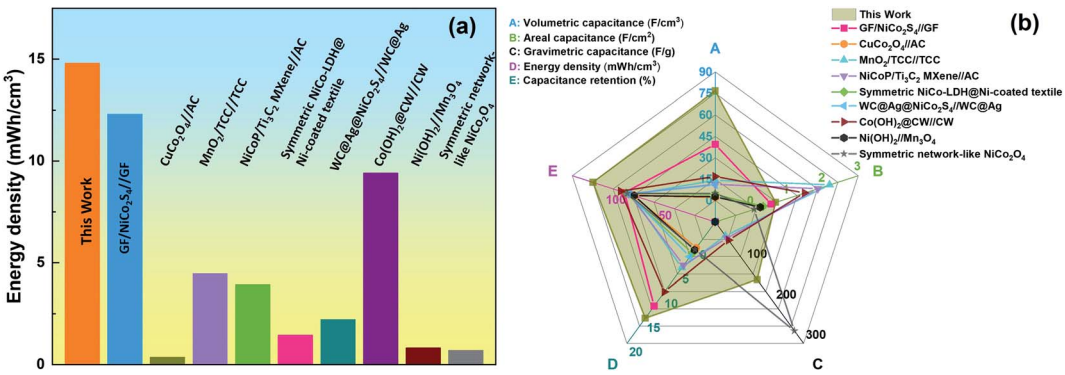

Fig. 6 (a) Comparison of the energy storage performance between our NiCo-LDH@Ni-NTNW//AC HSC and other previously reported supercapacitors. (b) Radar plots of the overall device performance and that of recently reported symmetric, asymmetric, and hybrid supercapacitors.

hybrid devices, with outstanding volumetric energy density, encompassing GF/$NiCo_2S_4$//CF (12.3 mWh cm^{-3}),[19] MnO_2/TCC//TCC (9.4 mWh cm^{-3}),[75] WC@Ag@$NiCo_2S_4$//WC@Ag (3.93 mWh cm^{-3}),[81] Co_9S_8//Co_3O_4@RuO_2 (1.44 mWh cm^{-3}),[73] symmetric NiCo-LDH@Ni-coated textile (1.25 mWh cm^{-3}),[82] NiCoP/Ti_3C_2 MXene//AC (2.2 mWh cm^{-3}),[74] $Co(OH)_2$@CW//CW (14.1 mWh cm^{-3}),[72] $CuCo_2O_4$//AC (0.81 mWh cm^{-3}),[83] symmetric mesoporous network-like $NiCo_2O_4$ (0.69 mWh cm^{-3}),[84] and $Ni(OH)_2$//Mn_3O_4 (0.35 mWh cm^{-3}),[85] as represented in Table S2† and Fig. 6a.

A comprehensive comparison of the overall performance of our outstanding NiCo-LDH@Ni-NTNW//AC device with the recently reported state-of-the-art symmetric, asymmetric, and hybrid supercapacitors (mentioned above) in terms of volumetric, areal, and gravimetric capacitances, energy density, and capacitance retention is presented in the radar plots in Fig. 6b and Table S2.† It is obvious that the overall performance of the demonstrated HSC is superior in comparison with the other devices. Such remarkable performance is ascribed not only to the unique Ni network-based hierarchical structure which boosts the rapid electron transport at high current density through the highly conductive metallic core, but also the NiCo-LDH nanosheets decorating the core Ni network with its longitudinal pathways that accelerate the ion diffusion and enhance the accessibility of the electrolyte into the interior parts of the electrode and offer a larger number of active sites through its massive surface area.

4 Conclusions

In summary, a prolific approach has been developed to design a self-supported hierarchical structure as an electrode with superior volumetric energy storage capacity. Inspired by the pipe cactus shape, a free-standing NiCo-LDH@Ni-NTNW electrode has been fabricated using facile and cost-effective techniques, namely electroless plating and electrodeposition. The prepared 3D core–shell structure combines the advantages of the Ni network core such as high conductivity and a fast electron transfer rate with the synergy offered by the NiCo-LDH nanosheets in terms of increased redox-active sites and an active surface area. Moreover, the distinguished design of such a hierarchical paradigm provides a highly porous interconnected structure that accelerates the ion diffusion rate. Meanwhile, our NiCo-LDH@Ni-NTNW electrode delivers a superior volumetric capacity of 126.4 C cm^{-3} maintaining a good rate capability of 53% at a high current of 20 mA cm^{-2} and 106% capacity retention after 4000 cycles. More importantly, the ultrathin design of the electrode enabled the assembling of a promising HSC device (NiCo-LDH@Ni-NTNW//AC) for practical applications with outstanding performance in terms of volumetric capacitance, energy density, and capacitance retention. The device demonstrated a volumetric capacitance of 76.7 F cm^{-3} and a volumetric energy density of 14.7 mWh cm^{-3}, proving itself as a remarkable device among the best symmetric, asymmetric, and hybrid supercapacitors that demonstrate high volumetric energy density. Such a superb and well-designed electrode corroborates the advantages of the 3D hierarchical structure and offers a tunable route for the development of versatile electrode architectures through integrating different active materials, targeting high energy storage.

Author contributions

Khaled M. Amin: conceptualization, investigation, methodology, visualization, and writing – original draft. Konrad Krois: investigation and writing – review & editing. Falk Muench: writing – review & editing. Bastian J. M. Etzold: supervision and writing – review & editing. Wolfgang Ensinger: supervision and writing – review & editing.

Conflicts of interest

There are no conflicts to declare.

Acknowledgements

The authors would like to thank Ulrike Kunz (Physical Metallurgy Group, TU Darmstadt) for conducting TEM measurements. The authors also acknowledge the Structural Research Group at TU Darmstadt for providing access to their XRD instrument and the Dispersive Solids Group at TU Darmstadt for access to their Raman Spectrometer. Khaled M. Amin gratefully acknowledges the financial support provided by the Ministry of Higher Education & Scientific Research (Egypt) and DAAD (Germany) for his PhD scholarship under the GERLS program (Grant No. 57403037). Konrad Krois and Bastian J. M. Etzold acknowledge the financial support by the Federal Ministry of Education and Research of Germany within the project 03ZZ0346A.

Notes and references

1 Z. Xu, C. Du, H. Yang, J. Huang, X. Zhang and J. Chen, NiCoP@CoS tree-like core–shell nanoarrays on nickel foam as battery-type electrodes for supercapacitors, *Chem. Eng. J.*, 2021, **421**, 127871, DOI: 10.1016/j.cej.2020.127871.

2 F. Liu, L. Zeng, Y. Chen, R. Zhang, R. Yang, J. Pang, L. Ding, H. Liu and W. Zhou, Ni–Co–N hybrid porous nanosheets on graphene paper for flexible and editable asymmetric all-solid-state supercapacitors, *Nano Energy*, 2019, **61**, 18–26, DOI: 10.1016/j.nanoen.2019.04.003.

3 K. N. Dinh, Q. Liang, C. F. Du, J. Zhao, A. I. Y. Tok, H. Mao and Q. Yan, Nanostructured metallic transition metal carbides, nitrides, phosphides, and borides for energy storage and conversion, *Nano Today*, 2019, **25**, 99–121, DOI: 10.1016/j.nantod.2019.02.008.

4 C. Ye, Q. Qin, J. Liu, W. Mao, J. Yan, Y. Wang, J. Cui, Q. Zhang, L. Yang and Y. Wu, Coordination derived stable Ni–Co MOFs for foldable all-solid-state supercapacitors with high specific energy, *J. Mater. Chem. A*, 2019, **7**, 4998–5008, DOI: 10.1039/c8ta11948a.

5 Y. Wang, Z. Yin, G. Yan, Z. Wang, X. Li, H. Guo and J. Wang, New insight into the electrodeposition of NiCo layered double hydroxide and its capacitive evaluation, *Electrochim.*

Acta, 2020, **336**, 135734, DOI: 10.1016/j.electacta.2020.135734.

6 Y. Guo, X. Hong, Y. Wang, Q. Li, J. Meng, R. Dai, X. Liu, L. He and L. Mai, Multicomponent Hierarchical Cu-Doped NiCo-LDH/CuO Double Arrays for Ultralong-Life Hybrid Fiber Supercapacitor, *Adv. Funct. Mater.*, 2019, **29**, 1809004, DOI: 10.1002/adfm.201809004.

7 H. Liu, J. Zhu, Z. Li, Z. Shi, J. Zhu and H. Mei, Fe2O3/N doped rGO anode hybridized with NiCo LDH/Co(OH)2 cathode for battery-like supercapacitor, *Chem. Eng. J.*, 2021, **403**, 126325, DOI: 10.1016/j.cej.2020.126325.

8 Y. Ouyang, X. Xia, H. Ye, L. Wang, X. Jiao, W. Lei and Q. Hao, Three-Dimensional Hierarchical Structure ZnO@C@NiO on Carbon Cloth for Asymmetric Supercapacitor with Enhanced Cycle Stability, *ACS Appl. Mater. Interfaces*, 2018, **10**, 3549–3561, DOI: 10.1021/acsami.7b16021.

9 Y. Wu and C. Cao, The way to improve the energy density of supercapacitors: Progress and perspective, *Sci. China Mater.*, 2018, **61**(12), 1517–1526, DOI: 10.1007/s40843-018-9290-y.

10 X. He, R. Li, J. Liu, Q. Liu, R. R. chen, D. Song and J. Wang, Hierarchical FeCo2O4@NiCo layered double hydroxide core/shell nanowires for high performance flexible all-solid-state asymmetric supercapacitors, *Chem. Eng. J.*, 2018, **334**, 1573–1583, DOI: 10.1016/j.cej.2017.11.089.

11 X. Wang, Y. Fang, B. Shi, F. Huang, F. Rong and R. Que, Three-dimensional NiCo2O4@NiCo2O4 core–shell nanocones arrays for high-performance supercapacitors, *Chem. Eng. J.*, 2018, **344**, 311–319, DOI: 10.1016/j.cej.2018.03.061.

12 C. Li, J. Balamurugan, D. C. Nguyen, N. H. Kim and J. H. Lee, Hierarchical Manganese–Nickel Sulfide Nanosheet Arrays as an Advanced Electrode for All-Solid-State Asymmetric Supercapacitors, *ACS Appl. Mater. Interfaces*, 2020, **12**, 21505–21514, DOI: 10.1021/acsami.9b23346.

13 P. Bandyopadhyay, G. Saeed, N. H. Kim and J. H. Lee, Zinc–nickel–cobalt oxide@NiMoO4 core–shell nanowire/nanosheet arrays for solid state asymmetric supercapacitors, *Chem. Eng. J.*, 2020, **384**, 123357, DOI: 10.1016/j.cej.2019.123357.

14 J. Zhao, Z. Li, T. Shen, X. Yuan, G. Qiu, Q. Jiang, Y. Lin, G. Song, A. Meng and Q. Li, Oxygen-vacancy Bi2O3 nanosheet arrays with excellent rate capability and CoNi2S4 nanoparticles immobilized on N-doped graphene nanotubes as robust electrode materials for high-energy asymmetric supercapacitors, *J. Mater. Chem. A*, 2019, **7**, 7918–7931, DOI: 10.1039/c8ta11953h.

15 C. Chen, S. Wang, X. Luo, W. Gao, G. Huang, Y. Zeng and Z. Zhu, Reduced ZnCo2O4@NiMoO4·H2O heterostructure electrodes with modulating oxygen vacancies for enhanced aqueous asymmetric supercapacitors, *J. Power Sources*, 2019, **409**, 112–122, DOI: 10.1016/j.jpowsour.2018.10.066.

16 A. D. Deshmukh, A. R. Urade, A. P. Nanwani, K. A. Deshmukh, D. R. Peshwe, P. Sivaraman, S. J. Dhoble and B. K. Gupta, Two-Dimensional Double Hydroxide Nanoarchitecture with High Areal and Volumetric Capacitance, *ACS Omega*, 2018, **3**, 7204–7213, DOI: 10.1021/acsomega.8b00596.

17 P. Sundriyal and S. Bhattacharya, Textile-based supercapacitors for flexible and wearable electronic applications, *Sci. Rep.*, 2020, **10**(1), 1–15, DOI: 10.1038/s41598-020-70182-z.

18 W. Yuan, S. Zou, X. Liu, K. Liu, C. Lv, P. Xie, Y. Yin, Y. Li and Z. Wu, Scalable Cable-Type Lithium-Ion Supercapacitors with High Loading Mass and Promotional Volumetric Energy Density, *ACS Sustainable Chem. Eng.*, 2020, **8**, 16869–16877, DOI: 10.1021/acssuschemeng.0c05928.

19 W. Cai, T. Lai, J. Lai, H. Xie, L. Ouyang, J. Ye and C. Yu, Transition metal sulfides grown on graphene fibers for wearable asymmetric supercapacitors with high volumetric capacitance and high energy density, *Sci. Rep.*, 2016, **6**(1), 1–9, DOI: 10.1038/srep26890.

20 K. Krois, L. Hüfner, J. Gläsel and B. J. M. Etzold, Simulative Approach for Linking Electrode and Electrolyte Properties to Supercapacitor Performance, *Chem. Ing. Tech.*, 2019, **91**, 889–899, DOI: 10.1002/cite.201800198.

21 J. Zhu, L. Wei, Q. Liu and X. Kong, Room-temperature preparation of amorphous CuNi-hybrid nanorod array as a fast battery-type electrode for high performance supercapacitor, *Mater. Chem. Phys.*, 2020, **247**, 122786, DOI: 10.1016/j.matchemphys.2020.122786.

22 M. Zhang, H. Fan, X. Ren, N. Zhao, H. Peng, C. Wang, X. Wu, G. Dong, C. Long, W. Wang, Y. Gao, L. Ma, P. Wu, H. Li and X. Jiang, Study of pseudocapacitive contribution to superior energy storage of 3D heterostructure CoWO4/Co3O4 nanocone arrays, *J. Power Sources*, 2019, **418**, 202–210, DOI: 10.1016/j.jpowsour.2019.02.041.

23 C. Su, S. Xu, L. Zhang, X. Chen, G. Guan, N. Hu, Y. Su, Z. Zhou, H. Wei, Z. Yang and Y. Qin, Hierarchical CoNi2S4 nanosheet/nanotube array structure on carbon fiber cloth for high-performance hybrid supercapacitors, *Electrochim. Acta*, 2019, **305**, 81–89, DOI: 10.1016/j.electacta.2019.03.013.

24 L. Zhi, W. Zhang, L. Dang, J. Sun, F. Shi, H. Xu, Z. Liu and Z. Lei, Holey nickel–cobalt layered double hydroxide thin sheets with ultrahigh areal capacitance, *J. Power Sources*, 2018, **387**, 108–116, DOI: 10.1016/j.jpowsour.2018.03.063.

25 Y. Wang, Z. Yin, Z. Wang, X. Li, H. Guo, J. Wang and D. Zhang, Facile construction of Co(OH)2@Ni(OH)2 core–shell nanosheets on nickel foam as three dimensional free-standing electrode for supercapacitors, *Electrochim. Acta*, 2019, **293**, 40–46, DOI: 10.1016/j.electacta.2018.10.025.

26 M. Zeiger, T. Ariyanto, B. Krüner, N. J. Peter, S. Fleischmann, B. J. M. Etzold and V. Presser, Vanadium pentoxide/carbide-derived carbon core–shell hybrid particles for high performance electrochemical energy storage, *J. Mater. Chem. A*, 2016, **4**, 18899–18909, DOI: 10.1039/c6ta08900c.

27 Ö. Budak, M. Geißler, D. Becker, A. Kruth, A. Quade, R. Haberkorn, G. Kickelbick, B. J. M. Etzold and V. Presser, Carbide-Derived Niobium Pentoxide with Enhanced Charge Storage Capacity for Use as a Lithium-Ion Battery Electrode, *ACS Appl. Energy Mater.*, 2020, **3**, 4275–4285, DOI: 10.1021/acsaem.9b02549.

28 S. Rafai, C. Qiao, M. Naveed, Z. Wang, W. Younas, S. Khalid and C. Cao, Microwave-anion-exchange route to ultrathin cobalt–nickel-sulfide nanosheets for hybrid

supercapacitors, *Chem. Eng. J.*, 2019, **362**, 576–587, DOI: 10.1016/j.cej.2019.01.059.

29 W. Younas, M. Naveed, C. Cao, S. Khalid, S. Rafai, Z. Wang, Y. Wu and L. Yang, Rapid and simplistic microwave assisted method to synthesise cobalt selenide nanosheets; a prospective material for high performance hybrid supercapacitor, *Appl. Surf. Sci.*, 2020, **505**, 144618, DOI: 10.1016/j.apsusc.2019.144618.

30 Q. Zhu, D. Zhao, M. Cheng, J. Zhou, K. Asare Owusu, L. Mai, Y. Yu, Q. Zhu, D. Zhao, M. Cheng, J. Zhou, Y. Yu, K. A. Owusu and L. Mai, A New View of Supercapacitors: Integrated Supercapacitors, *Adv. Energy Mater.*, 2019, **9**, 1901081, DOI: 10.1002/aenm.201901081.

31 S. C. Sekhar, G. Nagaraju and J. S. Yu, Conductive silver nanowires-fenced carbon cloth fibers-supported layered double hydroxide nanosheets as a flexible and binder-free electrode for high-performance asymmetric supercapacitors, *Nano Energy*, 2017, **36**, 58–67, DOI: 10.1016/j.nanoen.2017.04.019.

32 R. Patel, J. T. Park, M. Patel, J. K. Dash, E. B. Gowd, R. Karpoormath, A. Mishra, J. Kwak and J. H. Kim, Transition-metal-based layered double hydroxides tailored for energy conversion and storage, *J. Mater. Chem. A*, 2017, **6**, 12–29, DOI: 10.1039/c7ta09370e.

33 R. Patel, J. T. Park, M. Patel, J. K. Dash, E. B. Gowd, R. Karpoormath, A. Mishra, J. Kwak and J. H. Kim, Transition-metal-based layered double hydroxides tailored for energy conversion and storage, *J. Mater. Chem. A*, 2017, **6**, 12–29, DOI: 10.1039/c7ta09370e.

34 X. Li, D. Du, Y. Zhang, W. Xing, Q. Xue and Z. Yan, Layered double hydroxides toward high-performance supercapacitors, *J. Mater. Chem. A*, 2017, **5**, 15460–15485, DOI: 10.1039/c7ta04001f.

35 K. M. Amin, F. Muench, U. Kunz and W. Ensinger, 3D NiCo-Layered double Hydroxide@Ni nanotube networks as integrated free-standing electrodes for nonenzymatic glucose sensing, *J. Colloid Interface Sci.*, 2021, **591**, 384–395, DOI: 10.1016/j.jcis.2021.02.023.

36 H. Liang, J. Lin, H. Jia, S. Chen, J. Qi, J. Cao, T. Lin, W. Fei and J. Feng, Hierarchical NiCo-LDH@NiOOH core-shell heterostructure on carbon fiber cloth as battery-like electrode for supercapacitor, *J. Power Sources*, 2018, **378**, 248–254, DOI: 10.1016/j.jpowsour.2017.12.046.

37 M. Tian, W. Wang, Y. Wei and R. Yang, Stable high areal capacity lithium-ion battery anodes based on three-dimensional Ni–Sn nanowire networks, *J. Power Sources*, 2012, **211**, 46–51, DOI: 10.1016/j.jpowsour.2012.03.084.

38 F. Muench, Metal nanotube/nanowire-based unsupported network electrocatalysts, *Catalysts*, 2018, **8**, 597, DOI: 10.3390/catal8120597.

39 H. Guan, P. Cai, X. Zhang, Y. Zhang, G. Chen and C. Dong, Cu2O templating strategy for the synthesis of octahedral Cu2O@Mn(OH)2 core–shell hierarchical structures with a superior performance supercapacitor, *J. Mater. Chem. A*, 2018, **6**, 13668–13675, DOI: 10.1039/c8ta01828f.

40 T. Wang, S. Zhang, X. Yan, M. Lyu, L. Wang, J. Bell and H. Wang, 2-Methylimidazole-Derived Ni–Co Layered Double Hydroxide Nanosheets as High Rate Capability and High Energy Density Storage Material in Hybrid Supercapacitors, *ACS Appl. Mater. Interfaces*, 2017, **9**, 15510–15524, DOI: 10.1021/acsami.7b02987.

41 Y. Tao, L. Ruiyi, Z. Lin, M. Chenyang and L. Zaijun, Three-dimensional electrode of Ni/Co layered double hydroxides@NiCo2S4@graphene@Ni foam for supercapacitors with outstanding electrochemical performance, *Electrochim. Acta*, 2015, **176**, 1153–1164, DOI: 10.1016/j.electacta.2015.07.160.

42 H. Chen and S. Yang, Hierarchical nanostructures of metal oxides for enhancing charge separation and transport in photoelectrochemical solar energy conversion systems, *Nanoscale Horiz.*, 2016, **1**, 96–108, DOI: 10.1039/c5nh00033e.

43 Z. Qi and J. Weissmüller, Hierarchical nested-network nanostructure by dealloying, *ACS Nano*, 2013, **7**, 5948–5954, DOI: 10.1021/nn4021345.

44 S. M. Cha, G. Nagaraju, S. Chandra Sekhar and J. S. Yu, A facile drop-casting approach to nanostructured copper oxide-painted conductive woven textile as binder-free electrode for improved energy storage performance in redox-additive electrolyte, *J. Mater. Chem. A*, 2017, **5**, 2224–2234, DOI: 10.1039/c6ta10428b.

45 A. A. Ensafi, N. Ahmadi and B. Rezaei, Electrochemical preparation and characterization of a polypyrrole/nickel–cobalt hexacyanoferrate nanocomposite for supercapacitor applications, *RSC Adv.*, 2015, **5**, 91448–91456, DOI: 10.1039/c5ra17945a.

46 N. Zhao, H. Fan, M. Zhang, C. Wang, X. Ren, H. Peng, H. Li, X. Jiang and X. Cao, Preparation of partially-cladding NiCo-LDH/Mn3O4 composite by electrodeposition route and its excellent supercapacitor performance, *J. Alloys Compd.*, 2019, **796**, 111–119, DOI: 10.1016/j.jallcom.2019.05.023.

47 A. Noori, M. F. El-Kady, M. S. Rahmanifar, R. B. Kaner and M. F. Mousavi, Towards establishing standard performance metrics for batteries, supercapacitors and beyond, *Chem. Soc. Rev.*, 2019, **48**, 1272–1341, DOI: 10.1039/c8cs00581h.

48 L. Q. Mai, A. Minhas-Khan, X. Tian, K. M. Hercule, Y. L. Zhao, X. Lin and X. Xu, Synergistic interaction between redox-active electrolyte and binder-free functionalized carbon for ultrahigh supercapacitor performance, *Nat. Commun.*, 2013, **4**, 2923, DOI: 10.1038/ncomms3923.

49 T. Stohr, A. Fischer, F. Muench, M. Antoni, S. Wollstadt, C. Lohaus, U. Kunz, O. Clemens, A. Klein and W. Ensinger, Electroless Nanoplating of Pd–Pt Alloy Nanotube Networks: Catalysts with Full Compositional Control for the Methanol Oxidation Reaction, *ChemElectroChem*, 2020, **7**, 855–864, DOI: 10.1002/celc.201901939.

50 H. S. Jadhav, A. C. Lim, A. Roy and J. G. Seo, Room-Temperature Ultrafast Synthesis of NiCo-Layered Double Hydroxide as an Excellent Electrocatalyst for Water Oxidation, *ChemistrySelect*, 2019, **4**, 2409–2415, DOI: 10.1002/slct.201900063.

51 Q. Pan, F. Zheng, D. Deng, B. Chen and Y. Wang, Interlayer Spacing Regulation of NiCo-LDH Nanosheets with Ultrahigh

Specific Capacity for Battery-Type Supercapacitors, *ACS Appl. Mater. Interfaces*, 2021, **13**, 56692–56703, DOI: **10.1021/acsami.1c19320**.

52 F. Wang, S. Sun, Y. Xu, T. Wang, R. Yu and H. Li, High performance asymmetric supercapacitor based on Cobalt Nickle Iron-layered double hydroxide/carbon nanofibres and activated carbon, *Sci. Rep.*, 2017, 7(1), 1–11, DOI: **10.1038/s41598-017-04807-1**.

53 A. C. Gandhi, C. Y. Huang, C. C. Yang, T. S. Chan, C. L. Cheng, Y. R. Ma and S. Y. Wu, Growth mechanism and magnon excitation in NiO Nanowalls, *Nanoscale Res. Lett.*, 2011, **6**, 1–14, DOI: **10.1186/1556-276x-6-485**.

54 J. Chen, L. Zeng, X. Chen, T. Liao and J. Zheng, Preparation and characterization of bioactive glass tablets and evaluation of bioactivity and cytotoxicity in vitro, *Bioact. Mater.*, 2018, **3**, 315–321, DOI: **10.1016/j.bioactmat.2017.11.004**.

55 Y. Zhao, G. Fan, L. Yang, Y. Lin and F. Li, Assembling Ni–Co phosphides/carbon hollow nanocages and nanosheets with carbon nanotubes into a hierarchical necklace-like nanohybrid for electrocatalytic oxygen evolution reaction, *Nanoscale*, 2018, **10**, 13555–13564, DOI: **10.1039/c8nr04776f**.

56 D. Zha, H. Sun, Y. Fu, X. Ouyang and X. Wang, Acetate anion-intercalated nickel–cobalt layered double hydroxide nanosheets supported on Ni foam for high-performance supercapacitors with excellent long-term cycling stability, *Electrochim. Acta*, 2017, **236**, 18–27, DOI: **10.1016/j.electacta.2017.03.108**.

57 L. Liu, T. Guan, L. Fang, F. Wu, Y. Lu, H. Luo, X. Song, M. Zhou, B. Hu, D. Wei and H. Shi, Self-supported 3D NiCo-LDH/Gr composite nanosheets array electrode for high-performance supercapacitor, *J. Alloys Compd.*, 2018, **763**, 926–934, DOI: **10.1016/j.jallcom.2018.05.358**.

58 X. Cai, X. Shen, L. Ma, Z. Ji, C. Xu and A. Yuan, Solvothermal synthesis of NiCo-layered double hydroxide nanosheets decorated on RGO sheets for high performance supercapacitor, *Chem. Eng. J.*, 2015, **268**, 251–259, DOI: **10.1016/j.cej.2015.01.072**.

59 T. -C. Liu, W. G. Pell, B. E. Conway and S. L. Roberson, Behavior of Molybdenum Nitrides as Materials for Electrochemical Capacitors: Comparison with Ruthenium Oxide, *J. Electrochem. Soc.*, 1998, **145**, 1882–1888, DOI: **10.1149/1.1838571**.

60 F. Qian, P. C. Lan, M. C. Freyman, W. Chen, T. Kou, T. Y. Olson, C. Zhu, M. A. Worsley, E. B. Duoss, C. M. Spadaccini, T. Baumann and T. Y. J. Han, Ultralight Conductive Silver Nanowire Aerogels, *Nano Lett.*, 2017, **17**, 7171–7176, DOI: **10.1021/acs.nanolett.7b02790/suppl_file/nl7b02790_si_001.pdf**.

61 O. Picht, S. Müller, I. Alber, M. Rauber, J. Lensch-Falk, D. L. Medlin, R. Neumann and M. E. Toimil-Molares, Tuning the Geometrical and Crystallographic Characteristics of Bi2Te3 Nanowires by Electrodeposition in Ion-Track Membranes, *J. Phys. Chem. C*, 2012, **116**, 5367–5375, DOI: **10.1021/jp210491g**.

62 Y. Liu, N. Fu, G. Zhang, M. Xu, W. Lu, L. Zhou and H. Huang, Design of Hierarchical NiCo@NiCo Layered Double Hydroxide Core–Shell Structured Nanotube Array for High-Performance Flexible All-Solid-State Battery-Type Supercapacitors, *Adv. Funct. Mater.*, 2017, **27**, 1605307, DOI: **10.1002/adfm.201605307**.

63 K. N. Kang, A. Ramadoss, J. W. Min, J. C. Yoon, D. Lee, S. J. Kang and J. H. Jang, Wire-Shaped 3D-Hybrid Supercapacitors as Substitutes for Batteries, *Nano-Micro Lett.*, 2020, **12**, 1–13, DOI: **10.1007/s40820-019-0356-z**.

64 R. Li, Z. Hu, X. Shao, P. Cheng, S. Li, W. Yu, W. Lin and D. Yuan, Large Scale Synthesis of NiCo Layered Double Hydroxides for Superior Asymmetric Electrochemical Capacitor, *Sci. Rep.*, 2016, **6**(1), 1–9, DOI: **10.1038/srep18737**.

65 M. A. Abbasi, K. M. Amin, M. Ali, Z. Ali, M. Atif, W. Ensinger and W. Khalid, Synergetic effect of adsorption-photocatalysis by GO–CeO2nanocomposites for photodegradation of doxorubicin, *J. Environ. Chem. Eng.*, 2022, **10**, 107078, DOI: **10.1016/J.JECE.2021.107078**.

66 X. Zhang, L. Zhang, G. Xu, A. Zhao, S. Zhang and T. Zhao, Template synthesis of structure-controlled 3D hollow nickel–cobalt phosphides microcubes for high-performance supercapacitors, *J. Colloid Interface Sci.*, 2020, **561**, 23–31, DOI: **10.1016/j.jcis.2019.11.112**.

67 X. Y. Yu, H. Bin Wu, L. Yu, F. X. Ma and X. W. Lou, Rutile TiO2 submicroboxes with superior lithium storage properties, *Angew. Chem., Int. Ed.*, 2015, **54**, 4001–4004, DOI: **10.1002/anie.201411353**.

68 K. M. Amin and H. M. A. Amin, Carbon Nanoallotropes-Based Anticorrosive Coatings, in *Corrosion Protection of Metals and Alloys Using Graphene and Biopolymer Based Nanocomposites*, ed. H. M. A. Amin and A. Galal, CRC Press, 1st edn, 2020, pp. 81–98, DOI: **10.1201/9781315171364-8**.

69 G. Nagaraju, S. C. Sekhar, B. Ramulu and J. S. Yu, An Integrated Approach Toward Renewable Energy Storage Using Rechargeable Ag@Ni 0.67 Co 0.33 S-Based Hybrid Supercapacitors, *Small*, 2019, **15**, DOI: **10.1002/smll.201805418**.

70 W. Xu, Z. Jiang, Q. Yang, W. Huo, M. S. Javed, Y. Li, L. Huang, X. Gu and C. Hu, Approaching the lithium-manganese oxides' energy storage limit with Li2MnO3 nanorods for high-performance supercapacitor, *Nano Energy*, 2018, **43**, 168–176, DOI: **10.1016/j.nanoen.2017.10.046**.

71 S. Niu, Z. Wang, M. Yu, M. Yu, L. Xiu, S. Wang, X. Wu and J. Qiu, MXene-Based Electrode with Enhanced Pseudocapacitance and Volumetric Capacity for Power-Type and Ultra-Long Life Lithium Storage, *ACS Nano*, 2018, **12**, 3928–3937, DOI: **10.1021/acsnano.8b01459**.

72 Y. Wang, X. Lin, T. Liu, H. Chen, S. Chen, Z. Jiang, J. Liu, J. Huang and M. Liu, Wood-Derived Hierarchically Porous Electrodes for High-Performance All-Solid-State Supercapacitors, *Adv. Funct. Mater.*, 2018, **28**, 1806207, DOI: **10.1002/adfm.201806207**.

73 J. Xu, Q. Wang, X. Wang, Q. Xiang, B. Liang, D. Chen and G. Shen, Flexible Asymmetric Supercapacitors Based upon Co9S8 Nanorod//Co3O4@RuO2 Nanosheet Arrays on Carbon Cloth, *ACS Nano*, 2013, **7**, 5453–5462, DOI: **10.1021/nn401450s**.

74 L. Yu, W. Li, C. Wei, Q. Yang, Y. Shao and J. Sun, 3D Printing of NiCoP/Ti3C2 MXene Architectures for Energy Storage Devices with High Areal and Volumetric Energy Density, *Nano-Micro Lett.*, 2020, **12**, 1–13, DOI: **10.1007/s40820-020-00483-5**.

75 H. Wang, C. Xu, Y. Chen and Y. Wang, MnO2 nanograsses on porous carbon cloth for flexible solid-state asymmetric supercapacitors with high energy density, *Energy Storage Mater.*, 2017, **8**, 127–133, DOI: **10.1016/j.ensm.2017.05.007**.

76 N. F. Atta, K. M. Amin, H. A. Abd El-Rehim and A. Galal, Graphene prepared by gamma irradiation for corrosion protection of stainless steel 316 in chloride containing electrolytes, *RSC Adv.*, 2015, **5**, 71627–71636, DOI: **10.1039/c5ra11287g**.

77 A. Galal, K. M. Amin, N. F. Atta and H. A. Abd El-Rehim, Protective ability of graphene prepared by γ-irradiation and impregnated with organic inhibitor applied on AISI 316 stainless steel, *J. Alloys Compd.*, 2017, **695**, 638–647, DOI: **10.1016/j.jallcom.2016.11.081**.

78 D. Tian, N. Song, M. Zhong, X. Lu and C. Wang, Bimetallic MOF Nanosheets Decorated on Electrospun Nanofibers for High-Performance Asymmetric Supercapacitors, *ACS Appl. Mater. Interfaces*, 2019, **12**, 1280–1291, DOI: **10.1021/acsami.9b16420**.

79 R. Ramachandran, Y. Lan, Z. X. Xu and F. Wang, Construction of NiCo-Layered Double Hydroxide Microspheres from Ni-MOFs for High-Performance Asymmetric Supercapacitors, *ACS Appl. Energy Mater.*, 2020, **3**, 6633–6643, DOI: **10.1021/acsaem.0c00790**.

80 X. Sun, G. Wang, H. Sun, F. Lu, M. Yu and J. Lian, Morphology controlled high performance supercapacitor behaviour of the Ni–Co binary hydroxide system, *J. Power Sources*, 2013, **238**, 150–156, DOI: **10.1016/j.jpowsour.2013.03.069**.

81 F. Wang, X. Liu, G. Duan, H. Yang, J. Y. Cheong, J. Lee, J. Ahn, Q. Zhang, S. He, J. Han, Y. Zhao, I. D. Kim and S. Jiang, Wood-Derived, Conductivity and Hierarchical Pore Integrated Thick Electrode Enabling High Areal/Volumetric Energy Density for Hybrid Capacitors, *Small*, 2021, **17**, 1–10, DOI: **10.1002/smll.202102532**.

82 Y. M. Jeong, I. Son and S. H. Baek, Binder-free of NiCo-layered double hydroxides on Ni-coated textile for wearable and flexible supercapacitors, *Appl. Surf. Sci.*, 2019, **467–468**, 963–967, DOI: **10.1016/j.apsusc.2018.10.252**.

83 Q. Wang, D. Chen and D. Zhang, Electrospun porous CuCo2O4 nanowire network electrode for asymmetric supercapacitors, *RSC Adv.*, 2015, **5**, 96448–96454, DOI: **10.1039/c5ra21170k**.

84 S. Gao, F. Liao, S. Ma, L. Zhu and M. Shao, Network-like mesoporous NiCo2O4 grown on carbon cloth for high-performance pseudocapacitors, *J. Mater. Chem. A*, 2015, **3**, 16520–16527, DOI: **10.1039/c5ta02876k**.

85 J.-X. Feng, S.-H. Ye, X.-F. Lu, Y.-X. Tong and G.-R. Li, Asymmetric Paper Supercapacitor Based on Amorphous Porous Mn3O4 Negative Electrode and Ni(OH)2 Positive Electrode: A Novel and High-Performance Flexible Electrochemical Energy Storage Device, *ACS Appl. Mater. Interfaces*, 2015, **7**, 11444–11451, DOI: **10.1021/acsami.5b02157**.